

Predicting BN analogue of 8-16-4 graphyne: *In silico* insights into its structural, electronic, optical, and thermal transport properties

Isaac M. Felix,^{1,*} Jessé M. Pontes,^{2,†} Djardiel S. Gomes,^{2,‡} Thiago B. G. Guerra,^{2,§} Sérgio A. F. Azevedo,^{2,¶} Leonardo D. Machado,^{3,**} Lídia C. Gomes,^{1,††} and Raphael M. Tromer^{4,5,‡‡}

¹*Departamento de Física, Universidade Federal de Pernambuco, Recife-PE, 50670-901, Brazil*

²*Departamento de Física, Universidade Federal da Paraíba, João Pessoa-PB, 58051-970, Brazil*

³*Departamento de Física, Universidade Federal do Rio Grande do Norte, Natal-RN, 59078-970, Brazil*

⁴*School of Engineering, Mackenzie Presbyterian University, São Paulo SP. 01302-907, Brazil*

⁵*MackGraphe — Mackenzie Institute for Research in Graphene and Nanotechnologies, Mackenzie Presbyterian Institute, São Paulo SP. 01302-907, Brazil*

(Dated: June 24, 2024)

The boron nitride (BN) analogue of 8-16-4 graphyne, termed SBNyne, is proposed for the first time. Its physical properties were explored using first-principles calculations and classical molecular dynamics (MD) simulations. Thermal stability assessments reveal that SBNyne maintains structural integrity up to 1000 K. We found that SBNyne exhibits a wide indirect bandgap of 4.58 eV using HSE06 and 3.20 eV using PBE. It displays strong optical absorption in the ultraviolet region while remaining transparent in the infrared and visible regions. Additionally, SBNyne exhibits significantly lower thermal conductivity compared to h-BN. Phonon spectrum analysis indicates that out-of-plane phonons predominantly contribute to the vibrational density of states only at very low frequencies, explaining its low thermal conductivity. These findings expand the knowledge of BN-based 2D materials and open new avenues for their design and advanced technological applications.

I. INTRODUCTION

Ever since the groundbreaking synthesis of graphene¹, extensive research efforts have been devoted to exploring the vast potential of two-dimensional (2D) materials for applications in flat electronics^{2,3}. Graphene's remarkable properties have expanded the horizons of nanotechnology⁴⁻⁶, driving the search for alternative 2D carbon materials to overcome some of its limitations⁷⁻⁹. Various graphene derivatives with lower symmetries have been investigated, such as T-graphene¹⁰, Graphenylene^{11,12}, Phagraphene¹³, Penta-graphene¹⁴, Ψ -graphene¹⁵, DHQ-graphene¹⁶, PAI-graphene¹⁷, and Biphenylene¹⁸, to name a few. Other types of structural and hybridization configurations have also been widely addressed. The so-called graphynes are the first carbon allotropes containing single, double, and triple carbon-carbon bonds¹⁹⁻²². Graphyne structures can be viewed as derived from graphene by replacing some of the carbon bonds with acetylenic groups ($-C \equiv C-$)²⁰. It was predicted that graphyne would exhibit intriguing and unique electron-conducting^{21,23-26}, mechanical²⁷⁻²⁹, thermal³⁰, and optical^{21,31} properties.

Very recently, a novel 2D carbon allotrope named 8-16-4 graphyne, has been introduced^{32,33}. This single-atom-thick system derives its name from the distinctive structural feature of four carbon atoms interconnected in an octagonal shape, forming a 16-membered ring. The dynamic, mechanical, electronic, magnetic, optical, thermal, and thermodynamic properties of 8-16-4 graphyne have been investigated³²⁻³⁵. Bandyopadhyay et al.³² employed first-principles calculations to confirm the stability of 8-16-4 graphyne and propose a feasible chemical synthesis pathway for the material. Jafari et al.³⁴ stud-

ied how well transition metals adsorb to 8-16-4 graphyne. Their findings indicate 8-16-4 graphyne is a good candidate for use in catalysis and hydrogen storage because it can hold onto individual metal atoms and prevent them from clumping together. Peng et al.³⁵ have shown that temperature, vacancy concentration, and the presence of microcracks markedly affect the mechanical properties of 8-16-4 graphyne, providing valuable information for the design and application in flexible electronic devices. Tromer et al.³³ thoroughly explored the mechanical, structural, optical, and electrical properties of 8-16-4 graphyne via *ab initio* calculations. They discovered that its electrical properties remain stable even under moderate strains, making it highly promising for flexible electronic devices. They also picturesquely dubbed this system of Sun-graphyne because its unit cell's atomic arrangement bears a resemblance to drawings of the sun.

Computational materials science has paved the way for the theoretical exploration of 2D materials of BN, which exhibit topological similarities to their carbon-based counterparts³⁶. Some examples of these 2D BN structures are the h-BN^{37,38}, T-BN^{39,40}, phaBN⁴¹, BN graphenylene-like⁴², penta-BN⁴³, Ψ -BN⁴⁴, DHQ-BN⁴⁵, PAI-BN⁴⁶, and BN biphenylene-like^{47,48}. The BN analogues and isoelectronic equivalents of graphyne, referred to as BNynes, have also been proposed and investigated⁴⁹⁻⁵³. The combined network of sp^2 and sp hybridization states in a BNyne sheet alters the bonding characteristics between B and N atoms, resulting in unique chemical and physical properties, and has promising prospects and potential applications in nanoelectronics. For instance, Li et al.⁵¹ designed BNyne, BNdiyne, and BNtriyne by incorporating sp -hybridized BN bonds into a monolayer h-BN structure. They demonstrated that the band gap could be partly adjusted, ranging from

4.89 to 3.81 eV, by varying the length of the B–N chains. Zhang et al.⁴⁹ reported that the band gap of α , β , γ , and 6,6,12–BNynes is ranged from 4.12 to 4.23 eV and has a strong ultraviolet optical adsorption.

Despite the advancements made so far, the physical properties of the BN analogue of 8-16-4 graphyne remain unexplored. In this study, we employ *ab initio* calculations and classical molecular dynamics simulations to investigate the structural stability and electronic, optical, thermal transport, and vibrational (phonon) properties of the BN analogue of 8-16-4 graphyne, which will be designated here as Sun-BNyne (SBNyne) in reference to Sun-graphyne³³. We observed that SBNyne is dynamically stable and exhibits a wide bandgap. We found that SBNyne has a strong ultraviolet optical absorption, following the trend of other BN structures. Additionally, we predicted that the thermal conductivity of SBNyne is significantly lower than that of h-BN. Our findings provide valuable insights into the properties of SBNyne, expanding the understanding of 2D BN materials and their potential uses in nanoelectronics.

II. METHODS

To conduct the *ab initio* calculations, we utilized the SIESTA code, grounded in the formalism of Density Functional Theory (DFT)^{54–57}. The optimization of lattice geometry and electronic structure were performed with generalized gradient approximation of Perdew, Burke, and Ernzerhof (GGA-PBE)^{58,59}. Recognizing that GGA-PBE significantly underestimates the band gap, a portion of the electronic structure calculations was also carried out using the hybrid Heyd-Scuseria-Ernzerhof functional (HSE06)⁶⁰ in conjunction with the HONPAS package^{61,62}. The electron-ion interactions were described by Troullier-Martins conserved norm pseudopotentials^{63,64}, in the factored form of Kleinman-Bylander⁶⁵. We employed a mesh cutoff of 500 Ry for kinetic energy and a base double- ζ (DZP) set composed of numerical atomic orbitals with finite range. Brillouin zone integration utilized k -point sampling with the Monkhorst-Pack grid parameter set to $30 \times 30 \times 1$ ⁶⁶. During optimization, aiming for the lowest total energy, both lattice vectors and atomic positions were relaxed until the maximum force on each atom was below 0.01 eV/Å and the total energy difference was less than 10^{-5} eV. A 20 Å vacuum was applied along the z -direction to prevent interaction between neighboring cells. Additionally, we employ the SIESTA code for phonon dispersion calculations, as well as for conducting *ab initio* molecular dynamics and analyses of optical properties.

To perform optical calculations, we consider a standard external electric field of 1.0 V/Å along the z -direction. Using the Kramers-Kronig relation^{67,68} and Fermi's golden rule⁶⁹, we can obtain the real (ϵ_1) and imaginary (ϵ_2) parts of the dielectric constant. The real

part is expressed as:

$$\epsilon_1(\omega) = 1 + \frac{1}{\pi} P \int_0^\infty d\omega' \frac{\omega' \epsilon_2(\omega')}{\omega'^2 - \omega^2}, \quad (1)$$

where P represents the main value of the integral over ω' . The imaginary part is expressed considering interband optical transitions between valence (VB) and conduction bands (CB):

$$\epsilon_2(\omega) = \frac{4\pi^2}{\Omega\omega^2} \sum_{\substack{i \in \text{VB} \\ j \in \text{CB}}} \sum_k W_k |\rho_{ij}|^2 \delta(\epsilon_{kj} - \epsilon_{ki} - \hbar\omega), \quad (2)$$

where ω is the photon frequency, $|\rho_{ij}|$ is the dipole transition matrix element and W_k is the weight of the respective k -point in the reciprocal space. In Eq. (2), Ω is the volume of the unit cell. For 2D materials, Ω is defined differently compared to bulk materials. In bulk materials, the unit cell volume is typically the volume of the repeating unit cell in three-dimensional space. However, in 2D materials, the volume Ω_{2D} is defined as the area of the unit cell multiplied by its thickness, which is assumed to be approximately 3.35 Å for the h-BN⁷⁰. Therefore, for SBNyne the imaginary part was corrected (normalized) by multiplying Eq. (2) by $\frac{\Omega}{\Omega_{2D}}$.

Through ϵ_1 and ϵ_2 , it is possible to determine other properties, such as the absorption coefficient (α), reflectance (R), and refractive index (η):

$$\alpha(\omega) = \sqrt{2}\omega \left[(\epsilon_1^2(\omega) + \epsilon_2^2(\omega))^{1/2} - \epsilon_1(\omega) \right]^{1/2}, \quad (3)$$

$$R(\omega) = \left[\frac{(\epsilon_1(\omega) + i\epsilon_2(\omega))^{1/2} - 1}{(\epsilon_1(\omega) + i\epsilon_2(\omega))^{1/2} + 1} \right]^2, \quad (4)$$

$$\eta(\omega) = \frac{1}{\sqrt{2}} \left[(\epsilon_1^2(\omega) + \epsilon_2^2(\omega))^{1/2} + \epsilon_1(\omega) \right]^2. \quad (5)$$

Classical molecular dynamics modeling in this study was performed using the LAMMPS package⁷¹. We employed the Tersoff empirical potential⁷² with an optimized parameter set proposed by Sevik et al.⁷³, which has been widely used to model the thermal transport on BN systems^{74–77}. We employed reverse non-equilibrium molecular dynamics (rNEMD) simulations proposed by Müller-Plathe⁷⁸ to predict the thermal conductivity of SBNyne at room temperature (300 K). Simulations were performed for samples with different lengths to explore the length effect on the predicted thermal conductivity^{79,80}.

We applied periodic boundary conditions along the planar directions of the systems to remove the effect of free atoms at the edges. Each structure was first relaxed to zero stress along the planar direction at room temperature using a Nosé-Hoover thermostat and a barostat for 100 ps.

In the rNEMD method the system is divided in several slabs along its length, such that each slab contains at least ~ 200 atoms. Then, one swaps the kinetic energy of high velocity atoms in the end slabs with low velocity atoms in the central slab, imposing a heat current in the system. After a transient period, the average kinetic energy in the central slab is larger than the corresponding average in the extremities, originating a temperature gradient. The lattice thermal conductivity is calculated as the ratio between the heat current and the temperature gradient ∇T along the same direction, such that^{78,81}

$$\kappa = \frac{1}{|\nabla T|} \left[\frac{1}{2\Delta t A} \sum_{\text{swaps}} \Delta K \right], \quad (6)$$

where A is the cross-sectional area, Δt is the time interval over which the exchanges are imposed in the system, and ΔK is the difference in the kinetic energy of the particles in each swap. In all simulations, the equations of motion were integrated with the velocity-Verlet algorithm considering a time step of 0.25 femtoseconds, for a total time of 20 nanoseconds. Furthermore, the kinetic energy swaps were performed every 500 time steps.

III. RESULTS

A. Structural Stability

The SBNyne structure is composed of two distinct rings, each containing eight atoms. Its symmetric unit cell contains 16 atoms, with 8 being boron and 8 being nitrogen. After the optimization process, we observed that the unit cell vectors remained unchanged, with $|a_1| = |a_2| = 7.48 \text{ \AA}$, and the structure remained flat, without buckling. The schematic representation of the optimized SBNyne structure is shown in Figure 1.

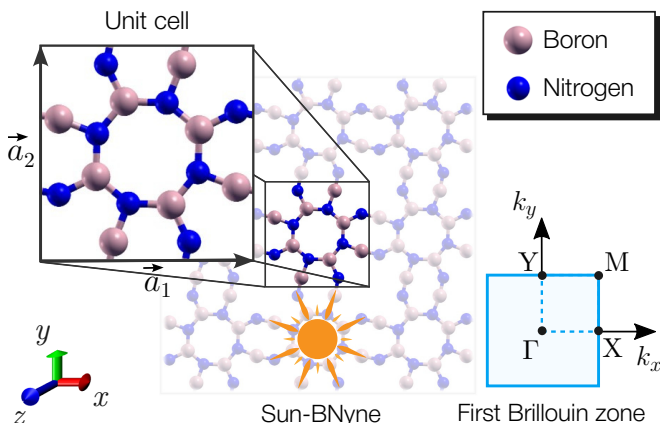


FIG. 1. Schematic representation of the SBNyne structure. The highlighted square represents the symmetric unit cell. The unit cell vectors are $|\vec{a}_1| = |\vec{a}_2| = 7.48 \text{ \AA}$. The boron and nitrogen atoms are represented by pink and blue spheres, respectively.

We calculated the energy stability of SBNyne through the formation energy. The analysis was conducted following a procedure based on the prior determination of appropriate chemical potentials at zero temperature, as described by Azevedo et al.^{82,83}. It's worth mentioning that additional DFT calculations were performed to determine all chemical potentials, utilizing procedures similar to those adopted in previous works⁸⁴.

According to this approach, the formation energy E_{form} for the monolayer SBNyne is given by:

$$E_{\text{form}} = \frac{E_T - N_B \mu_B - N_N \mu_N}{n_{\text{atom}}}, \quad (7)$$

where E_T is the total energy obtained from the SIESTA code, N_B and N_N are the quantities of boron and nitrogen atoms, respectively. μ_B and μ_N are the potentials of the two elements used. In order to obtain the chemical potentials, we utilized h-BN as references, i.e., $E_{\text{form}}^{\text{h-BN}} = 0$. Considering the fact that in a thermodynamic equilibrium of a h-BN system, the chemical potentials are subject to the subsequent condition $\mu_{\text{BN}} = \mu_B + \mu_N$, we found that the chemical potential of the B-N bond, boron and nitrogen species are $\mu_{\text{BN}} = -350.18 \text{ eV}$, $\mu_B = -80.03 \text{ eV}$ and $\mu_N = -270.15 \text{ eV}$, respectively. Finally, $n_{\text{atom}} = 16$ is the total number of atoms present in the structure.

Considering that the analysis of structural stability is based on the values obtained in the formation energy, it should be noted that lower values of E_{form} correspond to more stable structures, meaning they are more likely to be formed in a synthesis process⁸⁵. In this context, the SBNyne monolayer presents a value of 0.311 eV/atom , slightly higher than that obtained for h-BN monolayer⁸⁶, and of the same order as found for phaBN (0.335 eV/atom) and PAI-BN (0.365 eV/atom)^{41,46}. Thus, it can be inferred that SBNyne is relatively stable compared to other 2D boron nitride structures.

To assess dynamic stability, we computed the phonon dispersion spectrum using a 2×2 supercell, as illustrated in Figure 2. For this calculation, we followed the reciprocal space path $\Gamma (0,0) \rightarrow X (\frac{1}{2}, 0) \rightarrow M (\frac{1}{2}, \frac{1}{2}) \rightarrow Y (0, \frac{1}{2}) \rightarrow \Gamma (0,0)$. These points represent high-symmetry positions for the unit cell of the SBNyne monolayer. The absence of modes with negative (imaginary) frequencies in the phonon dispersion relation indicates that the crystalline structure of the SBNyne is dynamically stable.

We also conducted *ab initio* molecular dynamics (AIMD) simulations in 2×2 supercell to investigate the thermal stability of SBNyne at temperatures of 300 K and 1000 K. The calculations were performed using the SIESTA code with a time step of 1 fs in the NPT ensemble, employing a Parrinello-Rahman barostat to control pressure components in the plane and a Nose-Hoover thermostat to regulate temperature. This procedure is commonly applied to study the thermal stability of various materials⁸⁷⁻⁸⁹. The system evolved for 4 ps after heating the structure to the respective temperatures. In Figure 3, we present the time evolution of the total en-

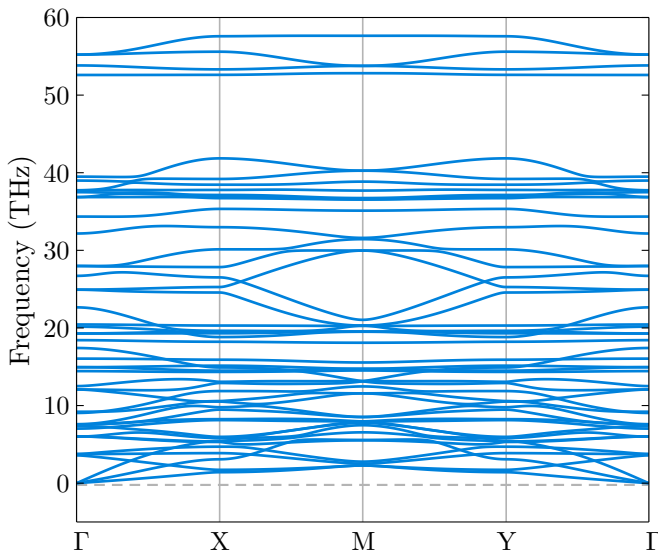


FIG. 2. The phonon frequencies are calculated in relation to the \mathbf{k} vectors for the system depicted in Figure 1.

ergy per atom in the SBNyne from AIMD simulations. The insets illustrate the top and side views for the AIMD snapshot of the SBNyne lattice in the final stage of the simulation. This figure shows that the SBNyne structure remains virtually unchanged at temperatures of 300 K and 1000 K, with only minor perturbations due to thermal fluctuations, suggesting that the SBNyne monolayer is stable at these temperatures.

B. Electronic properties

In Figure 4 (a), we present the electronic band structure of SBNyne along with its corresponding density of states calculated using the PBE functionals. It can be observed that SBNyne exhibits a wide bandgap semiconductor behavior with a bandgap of 3.20 eV. This value is significantly lower than that obtained for a monolayer of h-BN, which has a bandgap of approximately 6.0 eV. Additionally, SBNyne exhibits an indirect transition, where the maximum of the valence band is at the M point while the minimum of the conduction band is at the X point.

The results obtained using the HSE06 functional are shown in Figure 4 (b). We observed that with the functional correction, the bandgap of SBNyne increased to 4.58 eV, approaching the value of the bandgap of h-BN. Thus, SBNyne can be considered as an insulating material. Similarly, Mortazavi⁵³ reported that BN holey graphyne-like monolayers are an indirect insulator with large band gaps of 5.58 (4.20) eV according to the HSE06 (PBE) functional.

Figure 5 illustrates the projected density of states (PDOS), displaying the contribution of each atom to the electronic behavior of the SBNyne monolayer. It is evident that the p_z orbitals of the nitrogen atoms contribute significantly to the electronic states in the valence band,

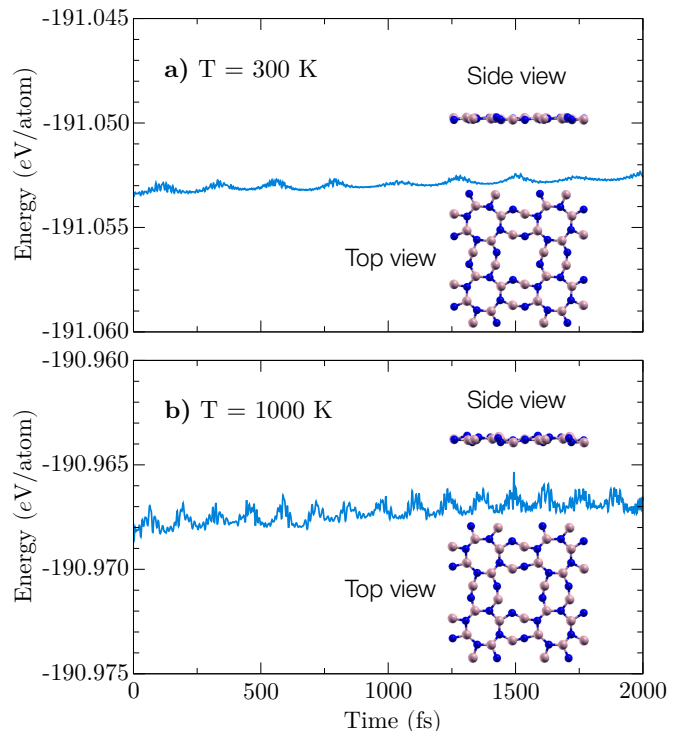


FIG. 3. Results from *ab initio* molecular dynamics calculations for the SBNyne structure at temperatures of 300 and 1000 K. The insets show the top and side views of the final AIMD snapshot at 2000 fs

while the states in the conduction band are associated with the $2p$ orbitals of boron atoms. For a detailed understanding of the contribution of each atom to the electronic behavior of SBNyne, the localized state density is also depicted in Figure 5. We can confirm that the states at the bottom of the conduction band are associated with the $2p$ orbitals of the boron atoms, while the states at the top of the valence band are associated with the p_z orbitals of the nitrogen atoms. This behavior is consistent with that observed in structures containing boron nitride, such as phaBN⁴¹ and PAI-BN⁴⁶.

C. Optical Properties

In Figure 6, we present the optical coefficients as a function of photon energy from 0 to 10 eV with an externally polarized electric field E applied in the z -direction ($E \parallel z$), i.e. E perpendicular to the plane. These calculations were performed using the PBE and HSE06 functionals. We hope that the optical properties studied here can be useful in the future for a direct comparison with experimental results.

In Figure 6 (a), we observe that absorption begins around 3.2 and 4.5 eV for the PBE and HSE06 functionals, respectively. This trend is expected since SBNyne is an insulating material. The various absorption peaks are in the ultraviolet region, where absorption intensities

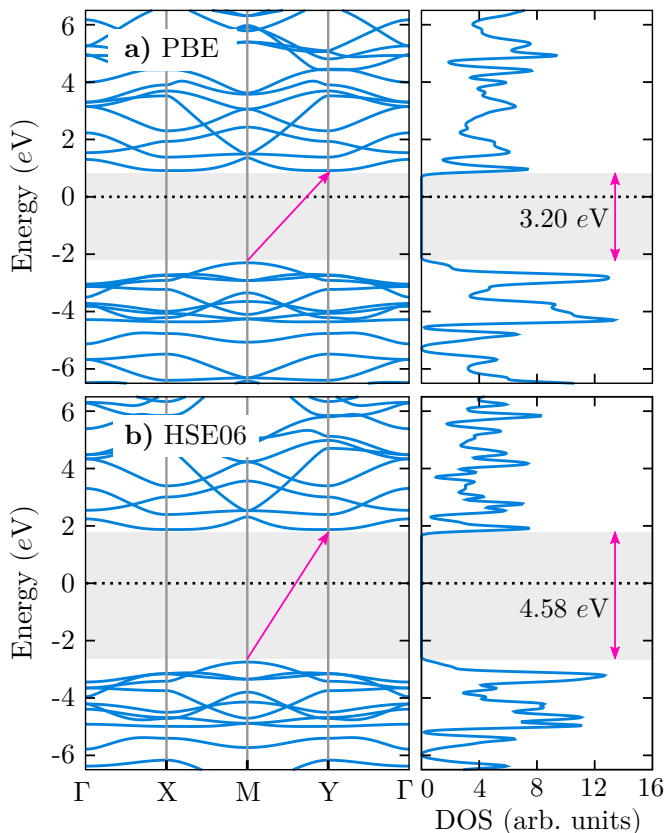


FIG. 4. Representation of the band structure and density of states of SBNyne using the PBE (a) and HSE06 (b) functionals. The Fermi level has been shifted to 0 eV.

can reach values of approximately $1.0 \times 10^{-6} \text{ cm}^{-1}$ for photon energies of ~ 5 to 7 eV . No absorption peaks are observed in the visible and infrared regions. Thus, SBNyne is completely transparent in these regions. These results are similar with the findings of Zhang et al.⁴⁹ for α , β , γ , and 6,6,12-BNynes structures and of Cao et al.⁵⁰ for BN-yne, -diyne, and -triyne. The refractive index is shown in Figure 6 (b). The value of the static refractive index (the refractive index value at zero energy) is ~ 1.8 (~ 2.4) for the HSE06 (PBE) functional. In Figure 6 (c), the reflectance results for the same functionals are presented. We can see that the reflectance of SBNyne is very low across the entire spectrum, with the highest peaks of reflectance located in the ultraviolet region. More specifically, for energies around $\sim 3.8 \text{ eV}$.

D. Lattice thermal conductivity

In materials with wide band gaps, the thermal transport properties are primarily governed by phonons. Phonons carry heat through the crystal lattice by transferring kinetic energy from one atom to another. Figure 7 shows the lattice thermal conductivity as a function of the length of the SBNyne samples. The data-point un-

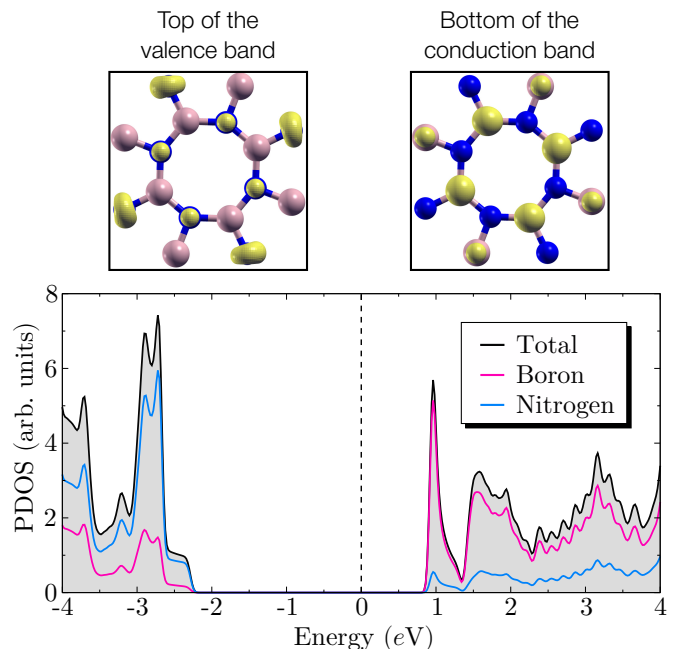


FIG. 5. Representation of the partial density of states (PDOS) of SBNyne. The Fermi level has been shifted to 0 eV. The local density of states (LDOS) associated with the bottom of the conduction band and the top of the valence band of SBNyne is shown above. Pink and blue spheres represent the boron and nitrogen atoms, respectively.

certainty was calculated based on the uncertainties of the average heat flux and temperature gradient using uncertainty propagation. In all cases, an uncertainty of less than 4% was observed. Due to size effects arising from the limitation of the phonon mean free path to the region between the heat reservoirs, the conductivity for a system of length L is expected to behave as^{90,91}:

$$\frac{1}{\kappa(L)} = \frac{1}{\kappa_\infty} \left(1 + \frac{\Lambda}{L} \right) \quad (8)$$

where κ_∞ is the intrinsic (length-independent) conductivity of the material, and Λ is the effective mean free path of the heat carriers. Therefore, by fitting the above expression to the simulation data obtained for systems of increasing length we can estimate both κ_∞ and Λ for the SBNyne. In this study, the intrinsic lattice thermal conductivity at room temperature is predicted to be $\sim 7.1 \text{ W/m-K}$. Meanwhile, the effective phonon mean free paths is $\sim 2.5 \text{ nm}$. The thermal conductivity value obtained for SBNyne is almost two orders of magnitude lower than the value obtained for h-BN sheets by Sevik et al.⁷³ using the tersoff potential with the same parameters. Furthermore, this value represents half the value obtained by Mortazavi⁵³ for BN holey graphyne-like monolayers via machine learning interatomic potentials.

The main advantage of the classical MD method in investigating the thermal transport of nanomaterials is its ability to simulate large molecular systems at an acceptable computational cost. Additionally, this method cap-

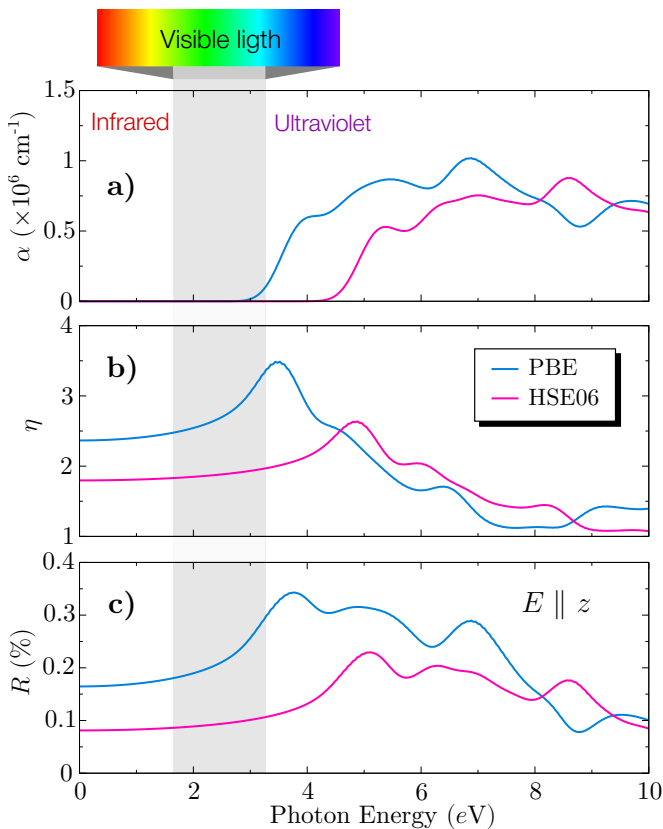


FIG. 6. (a) Absorption coefficient, (b) refractive index, and (c) reflectivity as a function of photon energy for the SBNyne monolayer. $E \parallel z$ denotes the polarization direction for the externally applied electric field.

tures all anharmonicities of lattice vibrations due to the predominantly classical potentials employed. However, there are drawbacks to the molecular dynamics method when compared to techniques based on the Boltzmann transport equation (BTE). These drawbacks include disregarding quantum effects and relying on the accuracy of the potential energy function, which is determined by the chosen force field. Additionally, MD is suitable for systems at moderately high temperatures since it assumes that phonons follow a Boltzmann distribution, which is not valid at low temperatures. Nevertheless, methods based on the BTE also have drawbacks. For instance, BTE can be computationally more intensive, especially when dealing with complex or large systems, due to the need to solve partial differential equations. Furthermore, BTE assumes the validity of the Boltzmann transport model, which may not be applicable across all temperature regimes and system sizes.

Very recently, Tromer et al.⁹² proposed a semi-empirical method capable of predicting the thermal conductivity of 2D materials with satisfactory accuracy and low computational cost, when compared to traditional computational methods. In this approach, the thermal conductivity at $T = 300$ K is obtained through a guessed

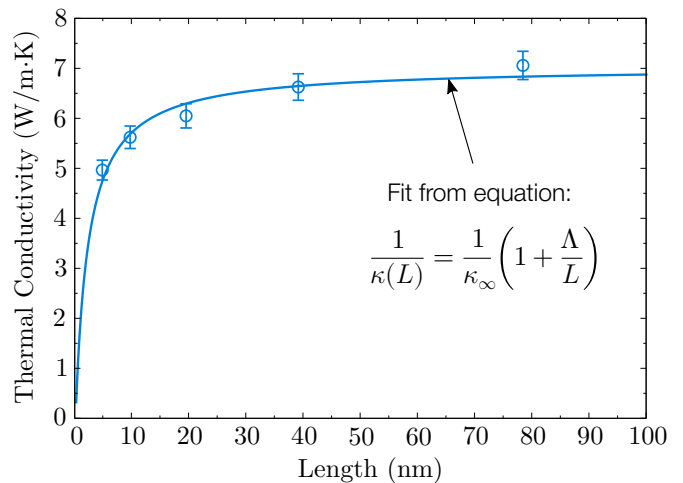


FIG. 7. Thermal conductivity of SBNyne as a function of sample length. Data points from RNEMD simulations and lines from Eq. (8).

expression:

$$\kappa_{\infty} = \frac{\bar{\nu} E_{VIB}}{L \delta T}, \quad (9)$$

where $\bar{\nu}$ is the average frequency, E_{VIB} is the vibration activation energy obtained from the Arrhenius plot, L is the lattice parameter of the minimum unit cell, and δT is a free parameter that depends on the type of system⁹². Given that the Tersoff potential utilized in the molecular dynamics simulations of the current study was originally parameterized for BN structures in general rather than specifically for SBNyne, we applied this approach to assess the thermal conductivity of SBNyne and compare it with the result obtained via the rNEMD method. Here, the parameters of Eq. (9) obtained for SBNyne were $\bar{\nu} = 23.59$ THz, $E_{VIB} = 9.62 \times 10^{-21}$ J, $L = 7.48$ Å, and $\delta T = 15$ K. By substituting these values into Eq. (9), we obtain a lattice thermal conductivity of $\kappa_{\infty} = 20.2$ W/mK for SBNyne. If we assume that the method described by Tromer et al.⁹² describes the thermal conductivity correctly, through calculation of relative error, we observe that the Tersoff potential parameterized by Sevik et al.⁷³ can underestimate the thermal conductivity of SBNyne by around 60%. In fact, for comparison purposes, the thermal conductivity of the BN holey graphyne-like monolayer obtained by Mortazavi⁵³ through machine learning interatomic potentials was around 14.0 W/mK. Applying the method of Tromer et al.⁹² for this system from Eq. (9) a value of 14.5 W/mK is obtained, indicating a relative error of less than 3.5%. The parameters of Eq. (9) found for BN holey graphyne-like monolayer were $\bar{\nu} = 24.75$ THz, $E_{VIB} = 9.62 \times 10^{-21}$ J, $L = 10.97$ Å, and $\delta T = 15$ K.

E. Phonon spectrum

To better understand the physical origins underlying of low thermal conductivity of SBNyne, we calculated the vibrational density of states (VDOS) via classical molecular dynamics employing the same potential that was used in the rNEMD method. The VDOS was obtained by post-processing 100 ps trajectories in which atomic velocities were recorded every 5 fs. The VDOS was computed by calculating the Fourier transform of the velocity autocorrelation function, as follows:

$$\text{VDOS}(\omega) = \int_0^\infty \frac{\langle \mathbf{v}(t) \cdot \mathbf{v}(0) \rangle}{\langle \mathbf{v}(0) \cdot \mathbf{v}(0) \rangle} \exp(-i\omega t) dt \quad (10)$$

where \mathbf{v} is the atomic velocity, ω is the angular frequency, and $\langle \mathbf{v}(t) \cdot \mathbf{v}(0) \rangle$ is the velocity autocorrelation function (VACF) which is normalized such that $\text{VACF}(t=0) = 1$.

Figure 8 shows calculated VDOS for the SBNyne. The panel (a) shows the individual contribution of boron and nitrogen atoms to the total VDOS. Boron atoms primarily contribute to the higher frequencies of the vibrational spectrum, above ~ 40 THz. This is due to the fact that boron atoms have a lower atomic mass compared to nitrogen atoms, resulting in higher vibration frequencies. In turn, nitrogen atoms mainly contribute to the lower frequencies of the spectrum, below ~ 10 THz. The interaction between boron and nitrogen atoms results in a very similar vibrational spectrum, mainly in a frequency range between ~ 10 and 35 THz.

The contribution of boron and nitrogen atoms to the vibrational spectrum of SBNyne is a typical aspect of the h-BN⁹³. However, the total VDOS of SBNyne presents different aspects compared to the VDOS of h-BN. For example, a pronounced peak near 55 THz resembles the typical optical peak of graphynes⁹⁴. Therefore, this fine structure reflects the nature of the chemical bonding between B and N atoms, in addition to the new symmetry of the crystal structure of SBNyne.

In nanomaterials, heat transport often benefits more from phonons with lower frequencies (longer wavelengths). These phonons experience fewer scattering events as they travel through the material due to their longer wavelengths, enabling them to carry more energy over longer distances and consequently contributing more significantly to thermal conductivity. Figure 8 (b) shows both the in-plane and the out-of-plane contributions to the total VDOS. It's noteworthy that out-of-plane phonons predominantly contribute to the VDOS only in the very low-frequency regime (< 1.5 THz). This dominance in the low-frequency regime may explain the low thermal conductivity of SBNyne in comparison to h-BN. In fact, previous studies have recognized the fundamental role of out-of-plane phonon oscillations (flexural modes) in the thermal transport in 2D materials^{95,96}. Finally, the Figure 8 (b) shows that high-frequency optical phonons are mostly dominated by in-plane vibrations.

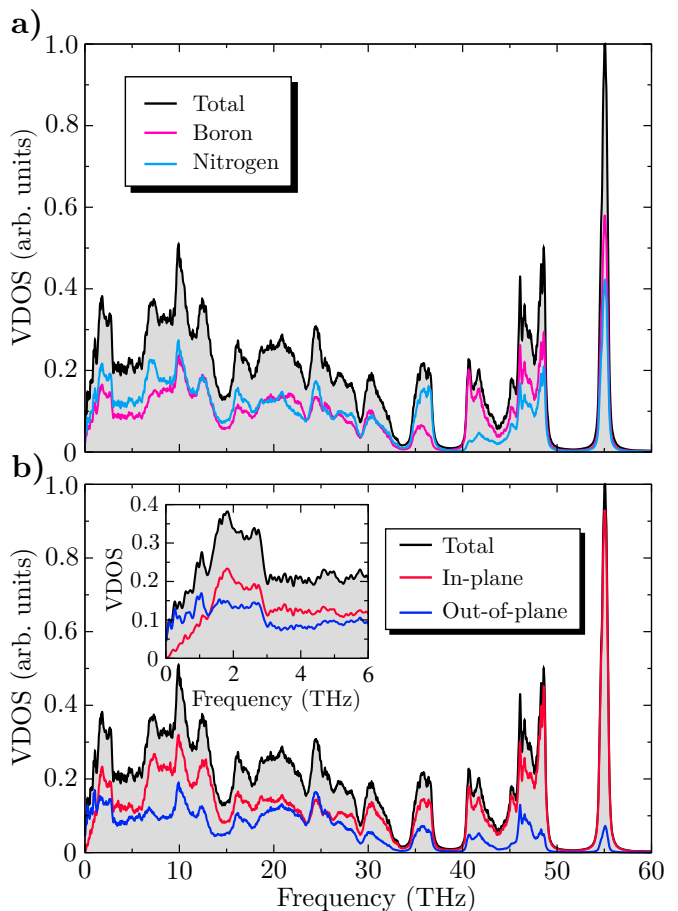


FIG. 8. Calculated VDOS for SBNyne sheets at room temperature. (a) Individual contribution of B and N atoms to the total VDOS. (b) Projected onto the in-plane and the out-of-plane direction.

IV. CONCLUSION

In summary, we conducted first-principles calculations using density functional theory to investigate the structural, electronic, and optical properties of the SBNyne structure. We observed a slight difference in energy stability between SBNyne and the h-BN monolayer. Phonon dispersion calculations revealed only positive frequencies in the phonon spectrum, indicating the system is dynamically stable. Furthermore, the structure remained stable during *ab initio* molecular dynamics simulations, even at temperatures exceeding 1000 K. From electronic calculations using the HSE06 (PBE) functional, we determined that SBNyne presents a wide indirect bandgap of 4.58 (3.20) eV. Regarding optical properties, we found that SBNyne is transparent to visible and infrared light, with the highest absorption peaks occurring in the ultraviolet region. Additionally, the reflectivity levels of the structure are very low.

The thermal transport properties of SBNyne were investigated, revealing much lower lattice thermal conduc-

tivity when compared to h-BN at room temperature. Furthermore, the vibrational density of states (VDOS) analysis provided insights into the phonon spectrum of SBNyne, indicating that out-of-plane phonons predominantly contribute to the VDOS in the very low-frequency regime (< 1.5 THz), which may explain the low thermal conductivity of the material compared to h-BN. Ultimately, we believe that SBNyne shows promise for various applications in nanoelectronics and optoelectronics, with its unique combination of electronic, optical, and thermal properties. These findings not only expand our understanding of 2D BN materials but also open up new

avenues for the design and application of SBNyne in advanced technologies.

ACKNOWLEDGEMENTS

The authors acknowledge financial support from the Brazilian agencies CNPq (grants 153604/2024-7 and 151333/2022-0), CAPES and FAPESQ. IMF and LCG acknowledge the INCT–Materials Informatics. IMF, LDM, and RMT acknowledge the support of the High Performance Computing Center at UFRN (NPAD/UFRN).

* isaac.equip@gmail.com

† jessempufcg@gmail.com

‡ djardiel95@gmail.com

§ thiagoguerra@servidor.uepb.edu.br

¶ sazevedo@fisica.ufpb.br

** leonardo@fisica.ufrn.br

†† lidia.cgomes@ufpe.br

‡‡ tromer@ifi.unicamp.br

¹ K. S. Novoselov, A. K. Geim, S. V. Morozov, D.-e. Jiang, Y. Zhang, S. V. Dubonos, I. V. Grigorieva, and A. A. Firsov, *Science* **306**, 666 (2004).

² G. Fiori, F. Bonaccorso, G. Iannaccone, T. Palacios, D. Neumaier, A. Seabaugh, S. K. Banerjee, and L. Colombo, *Nat. Nanotechnol.* **9**, 768 (2014).

³ A. K. Katiyar, A. T. Hoang, D. Xu, J. Hong, B. J. Kim, S. Ji, and J.-H. Ahn, *Chem. Rev.* **124**, 318 (2023).

⁴ A. K. Geim and K. S. Novoselov, *Nat. Mater.* **6**, 183 (2007).

⁵ F. Schwierz, *Nat. Nanotechnol.* **5**, 487 (2010).

⁶ F. Koppens, T. Mueller, P. Avouris, A. Ferrari, M. S. Vitiello, and M. Polini, *Nat. Nanotechnol.* **9**, 780 (2014).

⁷ A. N. Enyashin and A. L. Ivanovskii, *Phys. Status Solidi B* **248**, 1879 (2011).

⁸ H. Sun, S. Mukherjee, M. Daly, A. Krishnan, M. H. Karigerasi, and C. V. Singh, *Carbon* **110**, 443 (2016).

⁹ Q. Xie, L. Wang, J. Li, R. Li, and X.-Q. Chen, *Chinese Phys. B* **29**, 037306 (2020).

¹⁰ Y. Liu, G. Wang, Q. Huang, L. Guo, and X. Chen, *Phys. Rev. Lett.* **108**, 225505 (2012).

¹¹ A. T. Balaban and K. P. C. Vollhardt, *Open Org. Chem. J.* **5**, 117 (2011).

¹² Q. Song, B. Wang, K. Deng, X. Feng, M. Wagner, J. D. Gale, K. Müllen, and L. Zhi, *J. Mater. Chem. C* **1**, 38 (2013).

¹³ Z. Wang, X.-F. Zhou, X. Zhang, Q. Zhu, H. Dong, M. Zhao, and A. R. Oganov, *Nano Lett.* **15**, 6182 (2015).

¹⁴ S. Zhang, J. Zhou, Q. Wang, X. Chen, Y. Kawazoe, and P. Jena, *Proc. Natl. Acad. Sci.* **112**, 2372 (2015).

¹⁵ X. Li, Q. Wang, and P. Jena, *J. Phys. Chem. Lett.* **8**, 3234 (2017).

¹⁶ X. Wang, L. Chen, Z. Yuan, J. Rong, J. Feng, I. Muzammil, X. Yu, Y. Zhang, and Z. Zhan, *J. Mater. Chem. A* **7**, 8967 (2019).

¹⁷ X. Chen, A. Bouhon, L. Li, F. M. Peeters, and B. Sanyal, *Carbon* **170**, 477 (2020).

¹⁸ Q. Fan, L. Yan, M. W. Tripp, O. Krejčí, S. Dimosthenous, S. R. Kachel, M. Chen, A. S. Foster, U. Koert, P. Liljeroth, *et al.*, *Science* **372**, 852 (2021).

¹⁹ R. Baughman, H. Eckhardt, and M. Kertesz, *J. Chem. Phys.* **87**, 6687 (1987).

²⁰ F. Diederich, *Nature* **369**, 199 (1994).

²¹ J. Chen, J. Xi, D. Wang, and Z. Shuai, *J. Phys. Chem. Lett.* **4**, 1443 (2013).

²² X. Gao, H. Liu, D. Wang, and J. Zhang, *Chem. Soc. Rev.* **48**, 908 (2019).

²³ D. Malko, C. Neiss, F. Vines, and A. Görling, *Phys. Rev. Lett.* **108**, 086804 (2012).

²⁴ D. Malko, C. Neiss, and A. Görling, *Phys. Rev. B* **86**, 045443 (2012).

²⁵ M. Zhao, W. Dong, and A. Wang, *Sci. Rep.* **3**, 1 (2013).

²⁶ J. Kang, J. Li, F. Wu, S.-S. Li, and J.-B. Xia, *J. Phys. Chem. C* **115**, 20466 (2011).

²⁷ S. W. Cranford and M. J. Buehler, *Carbon* **49**, 4111 (2011).

²⁸ Q. Peng, W. Ji, and S. De, *Phys. Chem. Chem. Phys.* **14**, 13385 (2012).

²⁹ Y. Zhang, Q. Pei, and C. Wang, *Appl. Phys. Lett.* **101**, 081909 (2012).

³⁰ Y. Zhang, Q. Pei, and C. Wang, *Comput. Mater. Sci.* **65**, 406 (2012).

³¹ F. Diederich and M. Kivala, *Adv. Mater.* **22**, 803 (2010).

³² A. Bandyopadhyay, A. Majumdar, S. Chowdhury, R. Ahuja, and D. Jana, *Phys. Rev. B* **103**, 075137 (2021).

³³ R. M. Tromer, M. L. Pereira Junior, K. A. L. Lima, A. F. Fonseca, L. R. da Silva, D. S. Galvão, and L. A. Ribeiro Junior, *J. Phys. Chem. C* **127**, 12226 (2023).

³⁴ G. Jafari, A. Reisi-Vanani, and Z. Tabandeh, *Diam. Relat. Mater.* **142**, 110836 (2024).

³⁵ Q. Peng, Z. Huang, G. Chen, Y. Zhang, X. Zhang, X.-J. Chen, and Z. Hu, *Nanomaterials* **14**, 556 (2024).

³⁶ A. Enyashin and A. Ivanovskii, *Chem. Phys. Lett.* **509**, 143 (2011).

³⁷ K. Zhang, Y. Feng, F. Wang, Z. Yang, and J. Wang, *J. Mater. Chem. C*, **5**, 11992 (2017).

³⁸ A. M. Satawara, G. A. Shaikh, S. K. Gupta, and P. Gajjar, *Mater. Today Proc.* **47**, 529 (2021).

³⁹ R. Majidi, *Phys. E: Low-Dimens. Syst. Nanostruct.* **74**, 371 (2015).

⁴⁰ F. Nazneen, P. Mondal, N. A. Shahed, S. Khanom, M. K. Hossain, and F. Ahmed, *Comput. Theor. Chem.* **1224**, 114105 (2023).

- ⁴¹ J. Pontes, N. Frazão, D. L. Azevedo, and J. R. Lima, *Comput. Mater. Sci.* **188**, 110210 (2021).
- ⁴² E. Perim, R. Paupitz, P. Autreto, and D. Galvao, *J. Phys. Chem. C* **118**, 23670 (2014).
- ⁴³ J. Li, X. Fan, Y. Wei, and G. Chen, *Sci. Rep.* **6**, 1 (2016).
- ⁴⁴ F. Monteiro, K. Lima, and L. A. R. Junior, *Comput. Condens. Matter.* **37**, e00853 (2023).
- ⁴⁵ K. Lopes Lima, F. Lopes Mendonça, W. F. Giozza, R. T. de Sousa Júnior, and L. Ribeiro Junior, *Sci. Rep.* **14**, 2510 (2024).
- ⁴⁶ J. Pontes and S. Azevedo, *Chem. Phys. Impact.* **4**, 100074 (2022).
- ⁴⁷ N. N. Karaush, S. V. Bondarchuk, G. V. Baryshnikov, V. A. Minaeva, W.-H. Sun, and B. F. Minaev, *RSC Adv.* **6**, 49505 (2016).
- ⁴⁸ X.-D. Ma, Z.-W. Tian, R. Jia, and F.-Q. Bai, *Appl. Surf. Sci.* **598**, 153674 (2022).
- ⁴⁹ Y. Zhang, J. Yun, K. Wang, X. Chen, Z. Yang, Z. Zhang, J. Yan, and W. Zhao, *Comput. Mater. Sci.* **136**, 12 (2017).
- ⁵⁰ X. Cao, Y. Li, X. Cheng, and Y. Zhang, *Chem. Phys. Lett.* **502**, 217 (2011).
- ⁵¹ X.-D. Li and X.-L. Cheng, *Chem. Phys. Lett.* **694**, 102 (2018).
- ⁵² R. Majidi, *Chem. Phys.* **569**, 111874 (2023).
- ⁵³ B. Mortazavi, *Materials* **16**, 6642 (2023).
- ⁵⁴ J. M. Soler, E. Artacho, J. D. Gale, A. García, J. Junquera, P. Ordejón, and D. Sánchez-Portal, *J. Phys.: Condens. Matter* **14**, 2745 (2002).
- ⁵⁵ E. Artacho, D. Sánchez-Portal, P. Ordejón, A. Garcia, and J. M. Soler, *Phys. Status Solidi B* **215**, 809 (1999).
- ⁵⁶ P. Hohenberg and W. Kohn, *Phys. Rev.* **136**, B864 (1964).
- ⁵⁷ W. Kohn and L. J. Sham, *Phys. Rev.* **140**, A1133 (1965).
- ⁵⁸ J. P. Perdew, K. Burke, and M. Ernzerhof, *Phys. Rev. Lett.* **77**, 3865 (1996).
- ⁵⁹ J. P. Perdew, K. Burke, and M. Ernzerhof, *Phys. Rev. Lett.* **78**, 1396 (1997).
- ⁶⁰ J. Heyd, G. E. Scuseria, and M. Ernzerhof, *J. Chem. Phys.* **118**, 8207 (2003).
- ⁶¹ X. Qin, H. Shang, H. Xiang, Z. Li, and J. Yang, *Int. J. Quantum Chem.* **115**, 647 (2015).
- ⁶² H. Shang, L. Xu, B. Wu, X. Qin, Y. Zhang, and J. Yang, *Comput. Phys. Commun.* **254**, 107204 (2020).
- ⁶³ N. Troullier and J. L. Martins, *Phys. Rev. B* **43**, 1993 (1991).
- ⁶⁴ D. Hamann, M. Schlüter, and C. Chiang, *Phys. Rev. Lett.* **43**, 1494 (1979).
- ⁶⁵ L. Kleinman and D. Bylander, *Phys. Rev. Lett.* **48**, 1425 (1982).
- ⁶⁶ H. J. Monkhorst and J. D. Pack, *Phys. Rev. B* **13**, 5188 (1976).
- ⁶⁷ H. A. Kramers, in *Atti del Congresso Internazionale dei Fisici* (Como, Italy, 1927) pp. 1–13.
- ⁶⁸ R. d. L. Kronig, *J. Opt. Soc. Am.* **12**, 547 (1926).
- ⁶⁹ J. Tignon, P. Voisin, C. Delalande, M. Voos, R. Houdré, U. Oesterle, and R. Stanley, *Phys. Rev. Lett.* **74**, 3967 (1995).
- ⁷⁰ A. Falin, Q. Cai, E. J. Santos, D. Scullion, D. Qian, R. Zhang, Z. Yang, S. Huang, K. Watanabe, T. Taniguchi, *et al.*, *Nat. Commun.* **8**, 15815 (2017).
- ⁷¹ A. P. Thompson, H. M. Aktulga, R. Berger, D. S. Bolinteanu, W. M. Brown, P. S. Crozier, P. J. in't Veld, A. Kohlmeyer, S. G. Moore, T. D. Nguyen, *et al.*, *Comp. Phys. Comm.* **271**, 108171 (2022).
- ⁷² J. Tersoff, *Phys. Rev. Lett.* **61**, 2879 (1988).
- ⁷³ C. Sevik, A. Kinaci, J. B. Haskins, and T. Çağın, *Phys. Rev. B* **84**, 085409 (2011).
- ⁷⁴ H. Dong, P. Hirvonen, Z. Fan, and T. Ala-Nissila, *Phys. Chem. Chem. Phys.* **20**, 24602 (2018).
- ⁷⁵ X. Wu and Q. Han, *Comput. Mater. Sci.* **184**, 109938 (2020).
- ⁷⁶ V. Yamakov, C. Park, J. H. Kang, X. Chen, C. Ke, and C. Fay, *Comput. Mater. Sci.* **135**, 29 (2017).
- ⁷⁷ G. Loh and D. Baillargeat, *J. Appl. Phys.* **114**, 183502 (2013).
- ⁷⁸ F. Müller-Plathe, *J. Chem. Phys.* **106**, 6082 (1997).
- ⁷⁹ I. M. Felix and L. F. C. Pereira, *Carbon* **160**, 335 (2020).
- ⁸⁰ I. M. Felix and L. F. C. Pereira, *Int. J. Heat Mass Transf.* **186**, 122464 (2022).
- ⁸¹ L. F. C. Pereira and I. M. Felix, in *J. Phys.: Conf. Ser.*, Vol. 2241 (IOP Publishing, 2022) p. 012008.
- ⁸² S. Azevedo, *Phys. Lett. A* **325**, 283 (2004).
- ⁸³ S. Azevedo, M. S. Mazzoni, R. W. Nunes, and H. Chacham, *Phys. Rev. B* **70**, 205412 (2004).
- ⁸⁴ S. Azevedo, J. Kaschny, C. C. de Castilho, and F. de Brito Mota, *Eur. Phys. J. B* **67**, 507 (2009).
- ⁸⁵ S. Azevedo and J. Kaschny, *Eur. Phys. J. B* **86**, 1 (2013).
- ⁸⁶ B. Huang and H. Lee, *Phys. Rev. B* **86**, 245406 (2012).
- ⁸⁷ R. M. Tromer, A. Freitas, I. M. Felix, B. Mortazavi, L. Machado, S. Azevedo, and L. F. C. Pereira, *Phys. Chem. Chem. Phys.* **22**, 21147 (2020).
- ⁸⁸ E. Montes and U. Schwingenschlögl, *Phys. Rev. B* **94**, 035412 (2016).
- ⁸⁹ D. Silva, S. Azevedo, and J. Kaschny, *Eur. Phys. J. B* **94**, 1 (2021).
- ⁹⁰ P. K. Schelling, S. R. Phillpot, and P. Keblinski, *Phys. Rev. B* **65**, 144306 (2002).
- ⁹¹ I. M. Felix and L. F. C. Pereira, *Sci. Rep.* **8**, 1 (2018).
- ⁹² R. Tromer, I. Felix, L. Pereira, M. da Luz, L. R. Junior, and D. Galvao, *Phys. Chem. Chem. Phys.* **25**, 28703 (2023).
- ⁹³ B. Roonthe, V. Sharma, H. L. Kagdada, D. K. Singh, T. S. Dasgupta, and R. Ahuja, *Appl. Surf. Sci.* **533**, 147513 (2020).
- ⁹⁴ J. Wang, A.-J. Zhang, and Y. Tang, *J. Appl. Phys.* **118**, 195102 (2015).
- ⁹⁵ L. Lindsay, D. Broido, and N. Mingo, *Phys. Rev. B* **82**, 115427 (2010).
- ⁹⁶ A. Taheri, S. Pisana, and C. V. Singh, *Phys. Rev. B* **103**, 235426 (2021).